Effects of shape and size polydispersity on strength properties of granular materials

Duc-Hanh Nguyen, Emilien Azéma, Philippe Sornay, Farhang Radjai

Effects of shape and size polydispersity on strength properties of granular materials

Duc-Hanh Nguyen,[1,2,*] Emilien Azéma,[1,†] Philippe Sornay,[2,‡] and Farhang Radjai[1,3,§]
[1]*University of Montpellier, CNRS, LMGC, Place Eugène Bataillon, 34095 Montpellier, France*
[2]*CEA, DEN, DEC, SPUA, LCU, F-13108 Saint Paul lez Durance, France*
[3]*⟨MSE⟩², UMI 3466 CNRS-MIT, CEE, Massachusetts Institute of Technology, 77 Massachusetts Avenue, Cambridge, Massachusetts 02139, USA*
(Received 25 September 2014; published 18 March 2015)

By means of extensive contact dynamics simulations, we analyze the combined effects of polydispersity both in particle size and in particle shape, defined as the degree of shape irregularity, on the shear strength and microstructure of sheared granular materials composed of pentagonal particles. We find that the shear strength is independent of the size span, but unexpectedly, it declines with increasing shape polydispersity. At the same time, the solid fraction is an increasing function of both the size span and the shape polydispersity. Hence, the densest and loosest packings have the same shear strength. At the scale of the particles and their contacts, we analyze the connectivity of particles, force transmission, and friction mobilization as well as their anisotropies. We show that stronger forces are carried by larger particles and propped by an increasing number of small particles. The independence of shear strength with regard to size span is shown to be a consequence of contact network self-organization, with the falloff of contact anisotropy compensated by increasing force anisotropy.

DOI: 10.1103/PhysRevE.91.032203 PACS number(s): 45.70.−n, 83.80.Fg, 61.43.−j

I. INTRODUCTION

Most granular materials in their natural state or processed industrially are characterized by a broad range of particle shapes and sizes. For example, it is often a tedious task to describe in a simple way various shapes and size distributions of the fragments found in a coarse material generated by progressive fracturing of a rock or those of aggregates formed in a sintered powder. Although this *polydispersity* in the composition of granular materials is an obvious aspect of granular rheology, recent theoretical and experimental research has mainly focused on monodisperse systems composed of spherical particles. Hence, the effects of increasing departure from spherical shape and increasing size span on the structure and strength of granular materials are still largely open issues in granular research.

Some of these effects have recently been addressed by experiments and discrete numerical simulations [1–15]. For particle size, the most relevant effects arise from size span, which determines how in a packing the space is filled by particles of different sizes [2,16,17]. A broader size span leads to a denser packing, and it is commonly assumed that denser packings have a higher shear strength. However, contact dynamics (CD) simulations show that in cohesionless granular materials the shear strength is nearly independent of size span [4]. The shape of the particle size distribution is of second order compared to the size span but has not yet been the subject of systematic investigation. As for particle shapes, there is no unique description, and several disjoint shape parameters, such as roundedness and elongation, have been used to characterize particle shapes [18,19]. It was recently shown that the solid fraction and shear strength are mainly controlled by a generic parameter quantifying the difference between arbitrary particle shapes and spherical shape [9]. The shear strength is an increasing function of this parameter, whereas the packing fraction first increases and then declines, with a peak value well above the solid fraction of a disk packing.

In this paper, we numerically investigate the rheology of packings of irregular pentagonal particles and the effects of two polydispersity parameters: (i) size span and (ii) degree of shape irregularity. Although all the particles have pentagonal shapes, the degree of shape irregularity, defined from the angular positions of vertices, may be considered a shape polydispersity parameter that, together with size span, controls the structural properties of the granular assembly and its stress-strain behavior. In a previous paper, the rich structural properties of similar pentagon packings were studied for the same polydispersity parameters in dense states obtained by isotropic compaction [20]. The focus of this paper is the rheological properties of the same samples subjected to biaxial compression. The packings are analyzed in terms of their shear strength, solid fraction, particle connectivity, and fabric and force anisotropies as functions of the size and shape polydispersities.

We introduce in Sec. II the numerical approach, system characteristics, and loading parameters. In Sec. III we focus on the evolution of shear strength and packing fraction with polydispersity parameters. The microstructure is analyzed in Sec. IV in terms of connectivity, and fabric and force anisotropies. We conclude in Sec. V with a summary of the most important results of this work and possible routes to future research.

II. MODEL DESCRIPTION

Simulations were carried out by means of the CD method [21–24]. The CD method is a discrete element approach for the simulation of nonsmooth granular dynamics with contact laws expressing mutual exclusion and dry friction between particles and an implicit time integration scheme.

*dhnguyen2015@gmail.com
†emilien.azema@univ-montp2.fr
‡philippe.sornay@cea.fr
§franck.radjai@univ-montp2.fr

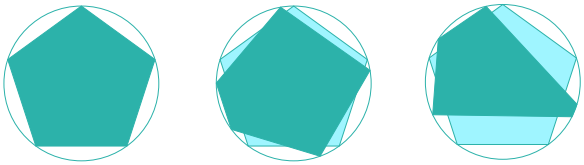

FIG. 1. (Color online) Regular pentagon ($\delta = 0$) deformed into irregular pentagons for two values of parameter δ.

Hence, this method is numerically unconditionally stable and suited to the simulation of frictional contacts between particles. It has been extensively used for the simulation of granular materials [2–4,7,10–13,25–29].

For a systematical investigation of the effect of polydispersity, strict procedures need to be used in order to generate particle shape and size with continuously varying parameters. Let us consider a regular pentagon such as that shown in Fig. 1. The angular position of a vertex k is given by $\theta^k = \theta_0 + 2k\pi/5$, where θ_0 is the position of the first vertex and k is an integer varying from 1 to 5. This regular pentagon can be transformed into an irregular pentagon by changing the angular positions of vertices k as

$$\theta^k = \theta_0 + k\frac{2\pi}{5} \pm \frac{\pi}{5} r_{[0,\delta]}, \tag{1}$$

where $r_{[0,\delta]}$ is a random variable in the range $[0,\delta]$. The parameter δ reflects the degree of shape irregularity and represents, in this sense, a *shape polydispersity parameter* for pentagons. Figures 1(b) and 1(c) show two examples of irregular pentagons for two values of δ.

The size of a pentagonal particle is defined by the diameter d of its circumscribed circle. The diameters of the particles are varied in the range of $[d_{\min}, d_{\max}]$ with a uniform distribution of particle volume fractions. We define the size span s of the distribution by [2]

$$s = \frac{d_{\max} - d_{\min}}{d_{\max} + d_{\min}}. \tag{2}$$

The case $s = 0$ corresponds to a monodisperse packing, whereas $s = 1$ corresponds to "infinite" polydispersity. In this work, s was systematically varied in the range $[0.01,0.9]$.

For each choice of the values of s and δ, 5000 particles are initially placed on a square network in a rectangular box of dimensions $l_0 \times h_0$ and deposited under the action of gravity g. Then the gravity is set to 0 and the packings are subjected to vertical compression applied on the upper wall, with the left, bottom, and right walls kept immobile. The friction coefficient between particles and with the walls is set to 0 during compression in order to obtain dense and isotropic packings. This procedure is stopped when a persistent contact force network in obtained and fluctuations around the mean values of the solid fraction and connectivity of the contact network remain below 0.1%. The morphology and structure of isotropic packings obtained by this protocol were analyzed in a previous paper by Nguyen *et al.* [20].

The isotropic samples are then subjected to vertical compression by downward displacement of the top wall at a constant velocity $\dot{y}$ for a constant confining stress σ_0 acting on the lateral walls. The friction coefficient μ between particles is set to 0.4, and that with the walls to 0. The zero friction with the walls prevents stress gradients such as those that lead to the Janssen effect [30]. The vertical shear rate $\dot{y}/y$ is low enough to ensure quasistatic conditions by reducing the inertia parameter I given by (in two dimensions) [31]

$$I = \dot{\varepsilon}\sqrt{\frac{m}{p}}, \tag{3}$$

where m is the mean particle mass and p is the mean pressure. The quasistatic limit is characterized by the condition $I \ll 1$. In our simulations, I was below 10^{-3}. Each sample is sheared until a steady state is reached with a nearly constant packing fraction.

Our system with 5000 particles is large enough to reflect the macroscopic behavior of the granular material in shear. By averaging the data over three independent simulations with different initial configurations, we get accurate values of the shear stress and packing fraction. The standard deviations calculated over several snapshots during the residual steady state and for three independent simulations are shown in Fig. 4 by error bars. We see that the variability of these data is quite small compared to their average values. In this sense, up to wall effects, which can, to some extent, affect the average values of stress deviator and packing fraction, our system mimics a representative volume element, as usually required for probing the intrinsic rheology of a material.

For data analysis, for each set of the values of s and δ, the mean behavior is obtained by ensemble averaging over three independent initial configurations. The results presented in this paper are based on 108 sheared samples for six values of size polydispersity $s \in [0.01,0.9]$ and for six values of shape polydispersity $\delta \in [0,1]$. Snapshots of packings obtained at the end of compression are shown in Fig. 2. We see that the resulting microstructures are very different for different values of s and δ. In the following sections, we are interested in the mechanical behavior of these different geometries. In particular, we see that the shear strength is the same in the samples in Figs. 2(a) and 2(b), which have the same shape polydispersity but different size polydispersities, but it is lower in the Fig. 2(c) sample, which has a larger shape polydispersity. For video samples of the simulations, see Ref. [44].

III. MECHANICAL BEHAVIOR AT THE MACROSCALE

The shear strength of a granular material is characterized by the coefficient of internal friction φ, which requires the stress tensor $\boldsymbol{\sigma}$ at any stage of deformation calculated from the contact network and forces. For the calculation of the stress tensor, we use the internal moment $\boldsymbol{M}^i$ of each particle i defined by [25,32]:

$$M^i_{\alpha\beta} = \sum_{c\in i} f^c_\alpha r^c_\beta, \tag{4}$$

where f^c_α is the α component of the force exerted on particle i at contact c, r^c_β is the β component of the position vector of the same contact c, and the summation runs over all contacts c of neighboring particles with particle i (denoted $c \in i$). It can be shown that the internal moment of a collection of rigid particles is the sum of the internal moments of individual particles. The

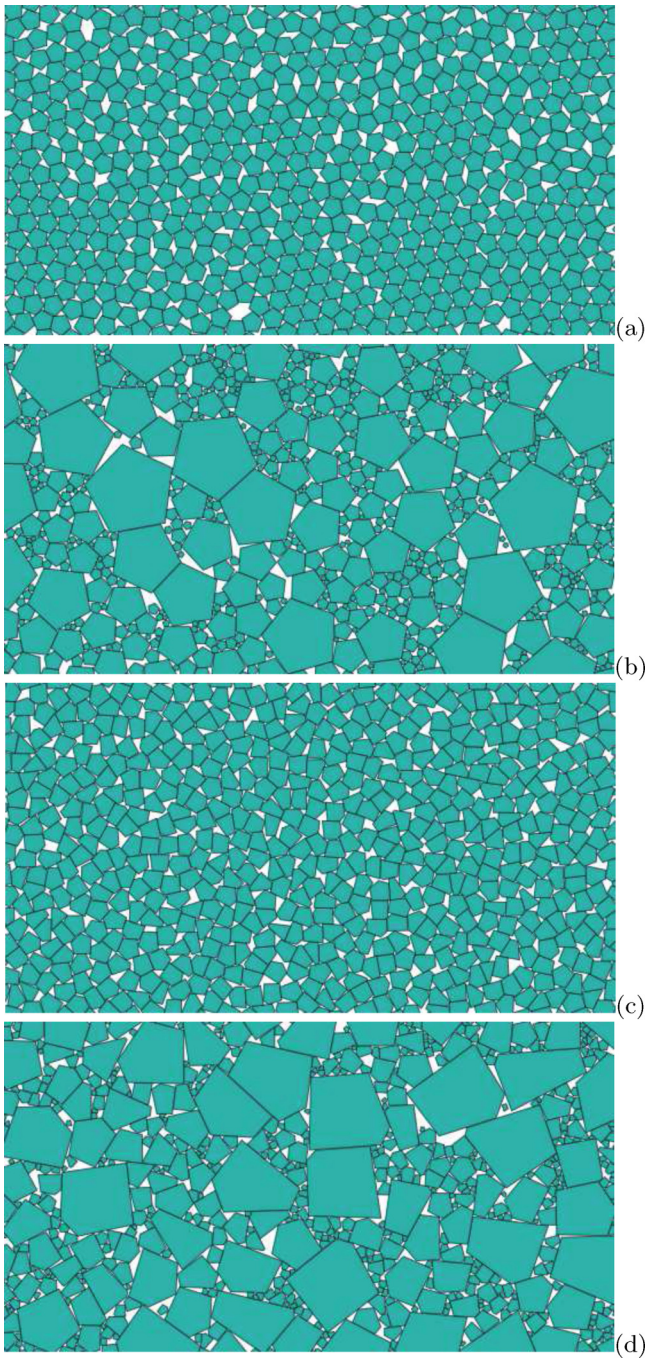

FIG. 2. (Color online) Snapshots of dense packings obtained at the end of compression, here for (a) $(s,\delta) = (0.01,0)$, (b) $(s,\delta) = (0.9,0)$, (c) $(s,\delta) = (0.01,1)$, and (d) $(s,\delta) = (0.9,1)$.

stress tensor $\boldsymbol{\sigma}$ in a portion of the material of volume V is simply the bulk density of internal moments given by [25,32]

$$\boldsymbol{\sigma} = \frac{1}{V}\sum_{i\in V} \boldsymbol{M}^i = \frac{1}{V}\sum_{c\in V} f_\alpha^c \ell_\beta^c, \tag{5}$$

where $\boldsymbol{\ell}^c$ is the intercenter vector joining the centers of the two touching particles at contact c. Note that the first summation runs over all particles, whereas the second summation involves the contacts in the volume, with each contact appearing only once. We extract the mean stress $p = (\sigma_1 + \sigma_2)/2$ and the

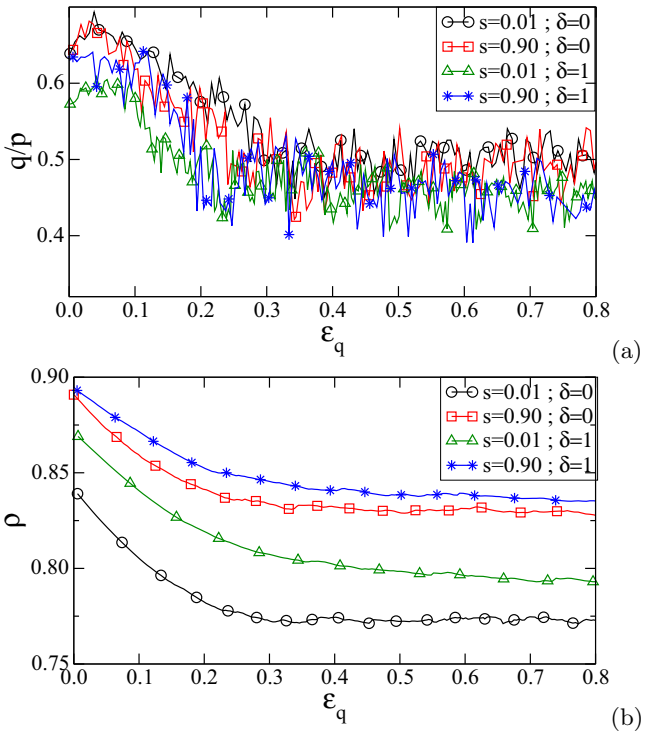

FIG. 3. (Color online) Normalized shear stress q/p (a) and solid fraction ρ (b) as a function of cumulative shear strain ε_q for different values of the polydispersity parameters s and δ.

stress deviator $q = (\sigma_1 - \sigma_2)/2$, where σ_1 and σ_2 are the principal stresses. The major principal direction during vertical compression is vertical.

The strain parameters are the cumulative vertical, horizontal, and shear strains ε_1, ε_2, and ε_q, respectively. By definition, we have

$$\varepsilon_1 = \int_{h_0}^{h} \frac{dh'}{h'} = \ln\left(1 + \frac{\Delta h}{h_0}\right), \tag{6}$$

where h_0 is the initial height and $\Delta h = h_0 - h$ is the total downward displacement, and

$$\varepsilon_2 = \int_{l_0}^{l} \frac{dl'}{l'} = \ln\left(1 + \frac{\Delta l}{l_0}\right), \tag{7}$$

where l_0 is the initial box width and $\Delta l = l - l_0$ is the total change of the box's width. The cumulative shear strain is then given by

$$\varepsilon_q = \varepsilon_1 - \varepsilon_2. \tag{8}$$

Figure 3 shows the normalized shear stress q/p and solid fraction ρ as a function of the shear strain ε_q for different values of polydispersity parameters. During biaxial deformation, the shear stress jumps initially to a high value before decreasing to a nearly constant value in the steady state. The friction angle $\sin\varphi^*$, defined from the mean value of q/p in the steady state [18], is independent of the initial state, and thus it represents the intrinsic shear strength of the material. All samples dilate during shear and ρ declines from its value $\rho^{\rm iso}$ (see Sec. II) in the initial isotropic state and levels off at a constant value ρ^* in the steady state. The samples undergo an

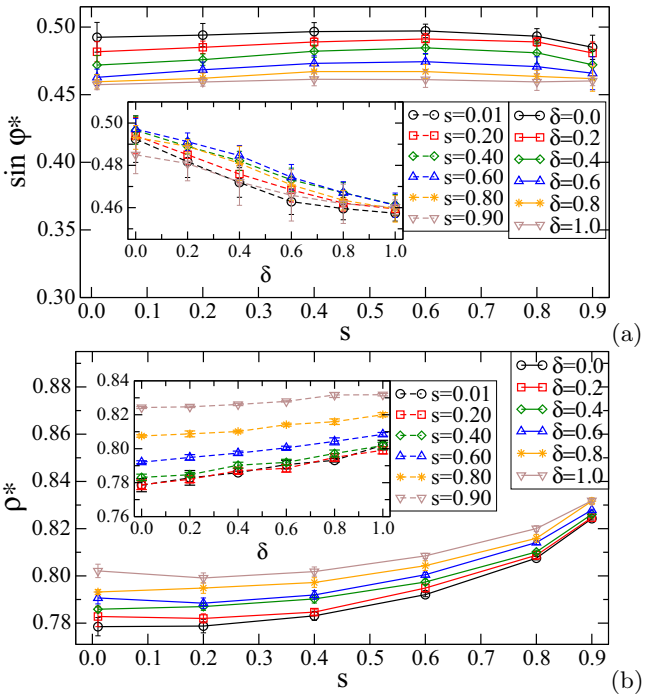

FIG. 4. (Color online) (a) Normalized friction angle $\sin\varphi^*$ as a function of s for all values of δ averaged in the steady state. Inset: q/p as a function of δ for all values of s. (b) Solid fraction ρ^* as a function of s for all values of δ averaged in the residual state. Inset: ρ^* as a function of δ for all values of s.

almost-homogeneous dilation at low shear strains and thus ρ decreases rapidly. At larger strains, dilation is localized within shear bands appearing throughout the system. As the shear bands develop at different locations inside the system, a nearly homogeneous density ρ^* is reached practically at $\varepsilon_q = 0.4$.

For our rigid particles the final solid fraction ρ^* is independent of the confining pressure, and like $\sin\varphi^*$ it is an intrinsic property of the material, reflecting basically the particle shape and size distributions as well as the friction coefficient between particles, which are the only parameters of our granular model.

Figure 4 shows the average values of $\sin\varphi^*$ and ρ^* as a function of both s and δ. For all shape polydispersities, the shear strength is almost independent of s. This finding thus extends to polygonal particles a similar behavior previously observed in the case of circular particles [4]. We also observe that, for all values of s, the shear strength declines as δ increases; see the inset in Fig. 4(a). This finding is unexpected because, even if the mean angularity (i.e., the mean exterior angle between sides) remains constant with δ, the particle shape anisometry increases, and it is known that the shear strength is an increasing function of particle elongation [7,33,34].

We also observe in Fig. 4(b) that the solid fraction increases with both size and shape polydispersities. In other words, our densest packings have the same shear strength as the loosest. This is also a rather counterintuitive behavior, as it is often believed that the shear strength in granular materials should increase with the solid fraction. Such paradoxical behaviors show that polydispersity in shape and size has profound effects on the granular microstructure.

IV. PARTICLE-SCALE ANALYSIS

The geometrical organization (i.e., texture) and force transmission in our simulated packings can be described in terms of different statistical descriptors. We consider here these geometrical and mechanical descriptors in order to quantify the combined effects of polydispersity parameters on the microstructure and their link with the shear strength.

A. Topology of the contact network

Figure 5 shows a snapshot of the contact network in the steady state for four samples. As in the case of random close packings analyzed in Ref. [20], the contact network topology varies strongly with both s and δ. The general impression is that the floating particles are mostly isolated for the highest level of shape polydispersity, whereas they tend to appear preferentially in the vicinity of other floating particles for the most regular shapes. In the same way, floating particles are mostly small for both shape and size polydispersities.

At lowest order, the connectivity of the contact network is characterized by the proportion X_f of floating particles and coordination number Z. Figure 6(a) shows X_f and z as a function of s for all values of δ. We see that X_f increases quickly from 0.15 to nearly 0.60 as s is increased, with an insignificant influence of δ. But surprisingly, the larger values of s lead to samples where less than half of the particles contribute to the contact network while such packings are the most compact ones. Indeed, high compactness implies a dense arrangement of the particles, where force chains involve a large number of particles in the contact network. This result is discussed below by considering the role of particle size in force transmission.

The inset in Fig. 6(a) shows the variation of Z as a function of s for all values of δ. In contrast to X_f, Z remains nearly constant as a function of s but increases with δ. For instance, for $s = 0.01$, it increases from 2.9 to 3.2, which is significant. This increase can be explained by the fact that the angular exclusions among the neighboring particles of a particle decrease due to the sharp corners of the most irregular particles. Figure 6(b) shows the average coordination number $\langle Z\rangle$ as a function of the reduced size d_r defined by

$$d_r = \frac{d - d_{\min}}{d_{\max} - d_{\min}}. \tag{9}$$

Interestingly, whatever the values of s and δ, we see a nearly linear relation between Z and d_r, with a slope that increases quickly with s and to a lesser extent with δ. Smaller particles have a lower number of contacts and therefore they are more likely to be excluded from the contact network. In contrast, larger particles are the most connected ones. In this way, larger polydisersity leads to enhanced diversification of topological configurations in the system. As shown in Fig. 5, the small particles usually occur in groups located in the space between larger particles. These groups can be entirely excluded from the contact network or, conversely, be involved and thus form a local structure with few contacts per particle.

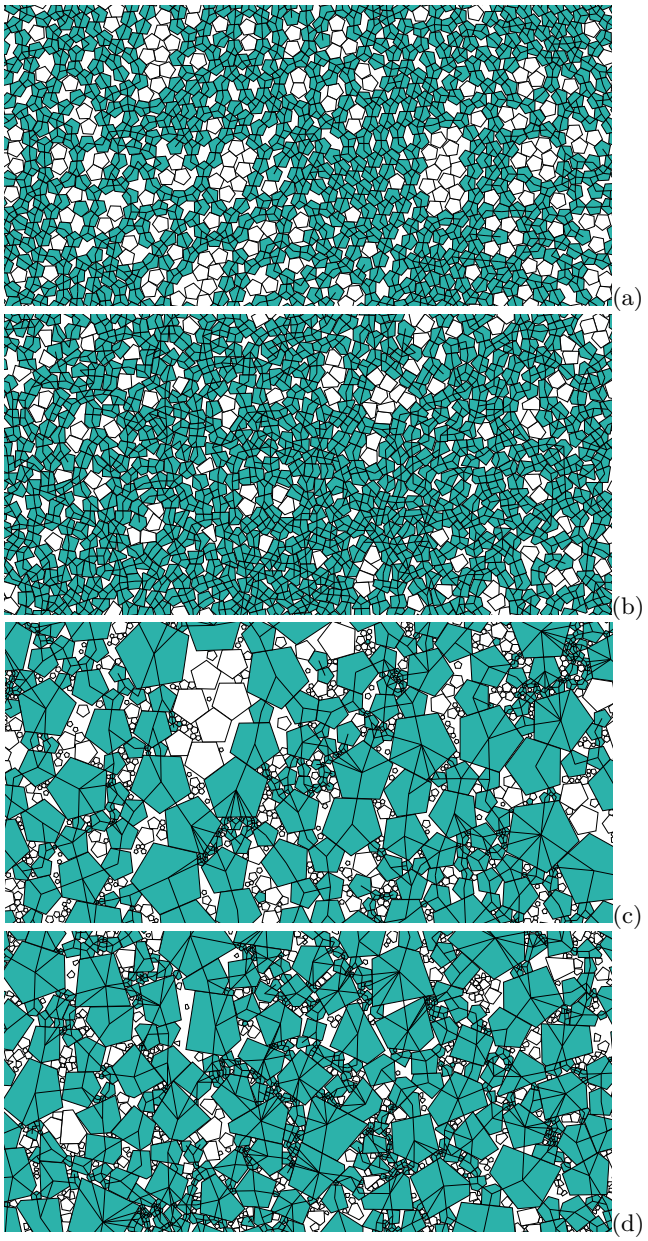

FIG. 5. (Color online) Snapshots of the contact network for (a) $(s,\delta) = (0.01,0)$, (b) $(s,\delta) = (0.9,0)$, (c) $(s,\delta) = (0.01,1)$, and (d) $(s,\delta) = (0.9,1)$. Floating particles (i.e., particles with one or no contacts) are shown in white, and contacts are represented by line segments joining the centers of mass of the particles to the contact points.

B. Force chains and friction mobilization

Figure 7 shows several maps of normal forces and friction mobilization at all contacts, defined as the ratio $I_\mu = \frac{|f_t|}{\mu f_n}$, where f_n and f_t are normal and tangential force, respectively. Visual inspection reveals that, at a high size span, stronger forces are supported by larger particles, whereas most mobilized contacts belong to the smallest particles. At a low size span, no peculiar organization of mobilized contacts is observed. Shape polydispersity does not seem to influence these features.

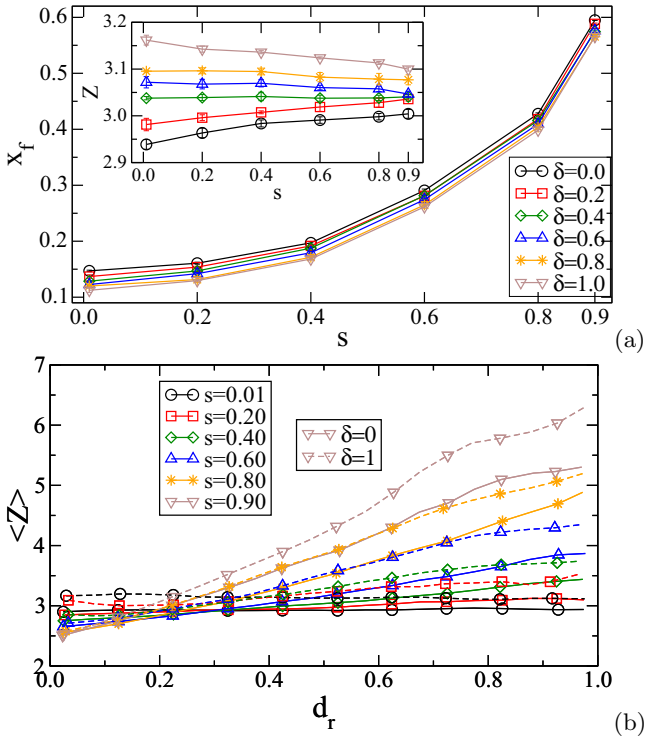

FIG. 6. (Color online) (a) Proportion X_f of floating particles as a function of size span for all values of shape polydispersity and (b) mean coordination number Z as a function of reduced diameter d_r for all values of size polydispersity.

Along with the force vector $\boldsymbol{f}$, the local geometry associated with the two contact neighbors is characterized by the intercenter vector $\boldsymbol{\ell}$ joining the particle centers; see Fig. 8. The length ℓ of intercenter vectors varies greatly throughout the network depending on the values of s and δ. For instance, for regular pentagons ($\delta = 0$) it is easy to show that

$$\frac{\ell}{R_{\max}} \in \left[2\frac{1-s}{1+s}\sin\frac{\pi}{3}; 2\right]. \tag{10}$$

The upper bound corresponds to the case where two pentagons are connected by a vertex-vertex contact. This is, however, a statistically rare event. The lower bound corresponds to side-side contacts between the smallest pentagons. The range of the values of ℓ becomes significant with increasing s and δ, and we expect the intercenter vector lengths to be correlated with the contact forces because of the contact configurations they represent.

Figure 9(a) shows the average normal force $\langle f_n\rangle_\ell$ as a function of ℓ for all values of s at $\delta = 0$ and $\delta = 1$ (inset). For $s < 0.4$, $\langle f_n\rangle_\ell$ is nearly equal to the mean force $\langle f_n\rangle$. But for larger size spans, allowing small particles to fit into the space between largest particles, we observe two well-defined zones: (i) the class of the shortest intercenter vectors $\ell < R_{\max}$, which concentrates, on average, the forces above the mean $\langle f_n\rangle$, and (ii) the class of the longest intercenter vectors ($\ell > R_{\max}$), which carry a considerably stronger force. This increase in the normal force with ℓ means that the larger particles, involved in longer intercenter vectors, capture stronger force chains, whereas small particles concentrate small forces. This

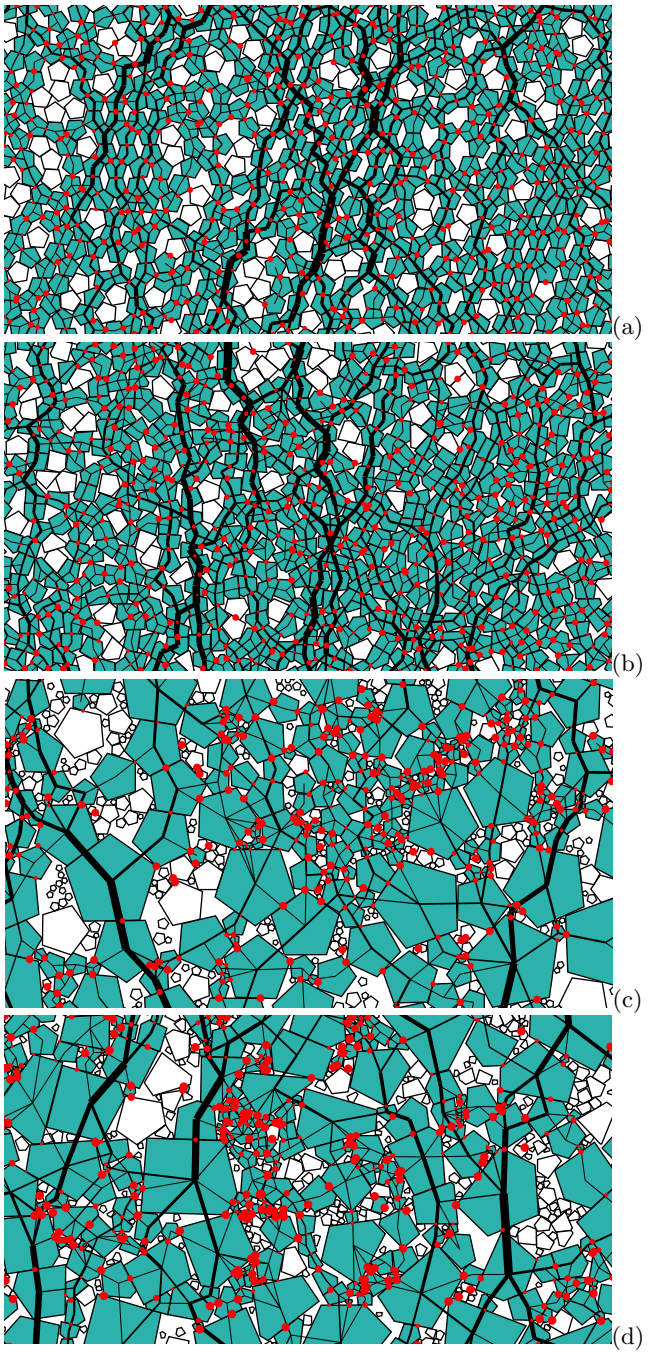

FIG. 7. (Color online) Snapshots of force-bearing particles for (a) $(s,\delta) = (0.01,0)$, (b) $(s,\delta) = (0.9,0)$, (c) $(s,\delta) = (0.01,1)$, and (d) $(s,\delta) = (0.9,1)$. Floating particles (i.e., particles with one or no contacts) are shown in white and normal forces are represented by the thickness of the segments joining the particle centers. The diameters of light-gray (red) circles are proportional to the friction mobilization at each contact.

behavior recalls the bimodal feature of stress transmission in granular materials [10,35,36], manifesting itself here in terms of particle sizes.

Figure 9(b) shows the average friction mobilization $\langle I_\mu \rangle_\ell$ as a function of ℓ for all values of s at $\delta = 0$ and $\delta = 1$ (inset). At a low size span and shape polydispersity, $\langle I_\mu \rangle_\ell$

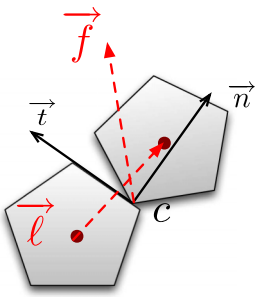

FIG. 8. (Color online) Local geometry.

is nearly equal to the global mobilization $\langle I_\mu \rangle$, except for very long intercenter lengths, where $\langle I_\mu \rangle_\ell > \langle I_\mu \rangle$. But at larger size spans the trend is reversed and we see that the class of shortest branches is increasingly mobilized in friction (i.e., $\langle I_\mu \rangle_\ell > \langle I_\mu \rangle$), whereas the distribution is nearly uniform for all other contacts. Furthermore, as shown in the inset in Fig. 9, this effect is enhanced with increasing shape polydispersity. This class belongs to the weak force network as shown previously, so that not only the friction mobilization $\langle I_\mu \rangle_\ell$ but also the number of highly mobilized contacts is larger in the weak force network. Note that a class of very weak forces was also evidenced in a packing of disks deposited under gravity and tilted towards its angle of stability [37,38] and in packings composed of elongated particles subjected to shear [10].

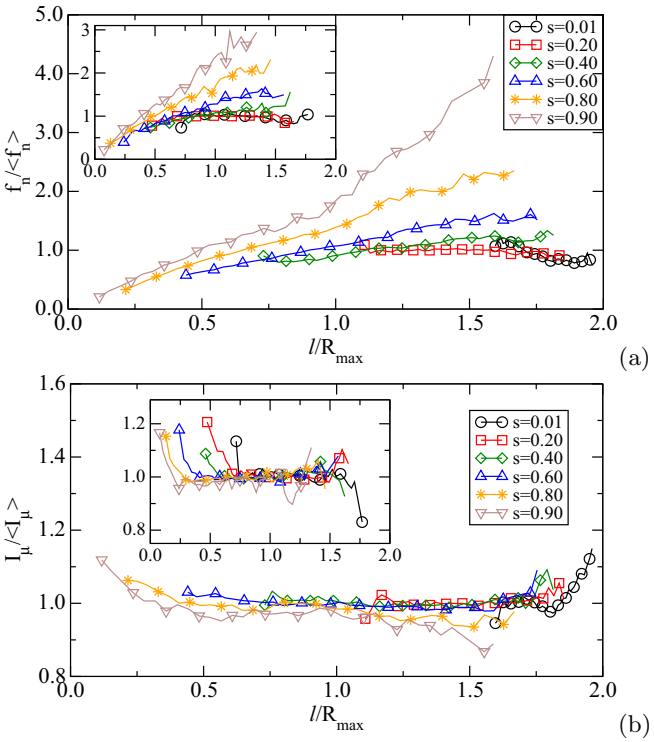

FIG. 9. (Color online) (a) Normal forces normalized by the mean $\langle f_n \rangle$ and (b) friction mobilization index I_μ normalized by the mean $\langle I_\mu \rangle$ as a function of the normalized intercenter length $\ell/R_{\max}$.

C. Anisotropy of the contact network

The most natural variables for the description of fabric anisotropy are the probability distribution function $P(\boldsymbol{n})$ of contact orientations $\boldsymbol{n}$ and the average intercenter vector $\langle \boldsymbol{\ell} \rangle(\boldsymbol{n})$ as a function of $\boldsymbol{n}$. In a similar vein, the force anisotropy can be characterized by the average contact force $\langle \boldsymbol{f} \rangle(\boldsymbol{n})$ as a function of $\boldsymbol{n}$ [3,7,12,39–41]. In two dimensions, the unit vector $\boldsymbol{n}$ is parametrized by a single angle θ, and the intercenter vector $\boldsymbol{\ell}$ and contact force $\boldsymbol{f}$ can be represented by their normal and tangential components. Thus, the probability density $P_\theta(\theta)$ of contact orientations θ, the angular averages of the components $\langle \ell_n \rangle(\theta)$ and $\langle \ell_t \rangle(\theta)$ of the intercenter vector, and the average components $\langle f_n \rangle(\theta)$ and $\langle f_t \rangle(\theta)$ of forces as a function of contact orientation θ provide a rich description of the anisotropic state of a granular material.

The above functions tend to take a simple unimodal shape, which can be well approximated by their truncated Fourier expansions [3,7,39],

$$P(\theta) = \frac{1}{2\pi}\{1 + a_c \cos 2(\theta - \theta_c)\}, \tag{11a}$$

$$\langle \ell_n \rangle(\theta) = \langle \ell_n \rangle\{1 + a_{\ell n} \cos 2(\theta - \theta_{\ell n})\}, \tag{11b}$$

$$\langle \ell_t \rangle(\theta) = \langle \ell_n \rangle a_{\ell t} \sin 2(\theta - \theta_{\ell t}), \tag{11c}$$

$$\langle f_n \rangle(\theta) = \langle f_n \rangle\{1 + a_{fn} \cos 2(\theta - \theta_{fn})\}, \tag{11d}$$

$$\langle f_t \rangle(\theta) = \langle f_n \rangle a_{ft} \sin 2(\theta - \theta_{ft}), \tag{11e}$$

where a_c is the contact orientation anisotropy, $a_{\ell n}$ is the normal branch anisotropy, $a_{\ell t}$ is the tangential branch anisotropy, a_{fn} is the normal force anisotropy, and a_{ft} is the tangential force anisotropy. The angles θ_c, $\theta_{\ell n}$, $\theta_{\ell t}$, θ_{fn}, and θ_{ft} are the corresponding privileged directions. These directions can all be different, but they nearly coincide with the principal stress direction θ_σ in a sheared granular material, as illustrated in Fig. 10 for different values of s and δ.

Figure 11 displays the anisotropy parameters, averaged in the steady state, as a function of s for all values of δ and as a function of δ for all values of s. We see that a_c declines as a function of both s and δ. The decrease in a_c in the steady state is compatible with the fact that the larger particles are surrounded by an increasing number of small particles as s and δ increase, as shown in Sec. IV A. At the same time, the normal branch length anisotropy $a_{\ell n}$ increases with s since the longest branch vectors occur between the largest particles, which tend to align themselves along strong force chains. It is remarkable that $a_{\ell n}$ is almost independent of δ, whereas $a_{\ell t}$ is independent of both s and δ. Geometrically, the anisotropy $a_{\ell t}$ reflects some degree of shape eccentricity or elongation of the particles [7,42]. The polydispersity parameters s and δ do not affect eccentricity.

The behavior of force anisotropies is quite similar. The normal force anisotropy a_{fn} increases slightly with s but is independent of δ. On the other hand, the friction force anisotropy a_{ft} remains independent of both s and δ. Note that the friction force anisotropy is proportional to the friction mobilization I_μ. Indeed, integrating Eq. (11a e) in the range $[0,\pi/2]$ yields $\langle I_\mu \rangle = 2a_{ft}/\mu$.

The anisotropy parameters a_c, $a_{\ell n}$, $a_{\ell t}$, a_{fn}, and a_{ft} are interesting not only as descriptors of the granular microstructure

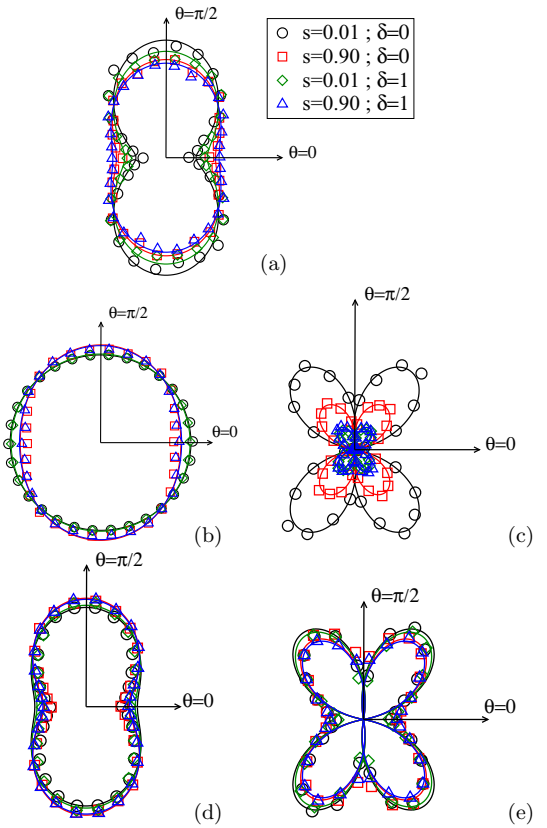

FIG. 10. (Color online) Polar representation of the functions (a) $P(\theta)$, (b) $\langle \ell_n \rangle(\theta)$, (c) $\langle \ell_t \rangle(\theta)$, (d) $\langle f_n \rangle(\theta)$, and (e) $\langle f_t \rangle(\theta)$ (symbols) and with truncated Fourier approximations (solid lines) for different values of s and δ.

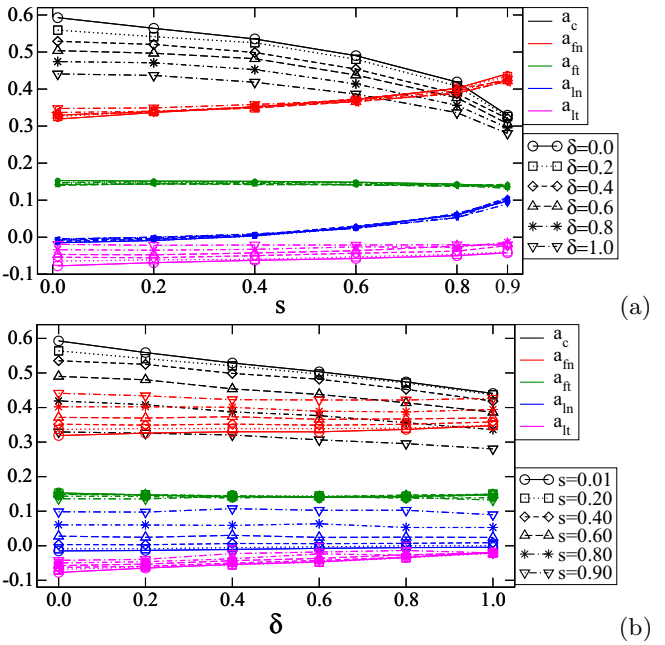

FIG. 11. (Color online) Evolution of state anisotropies (a) as a function of s for all values of δ and (b) as a function of δ for all values of s in the steady shear state. Error bars correspond to the standard deviation of the fluctuations in the steady state.

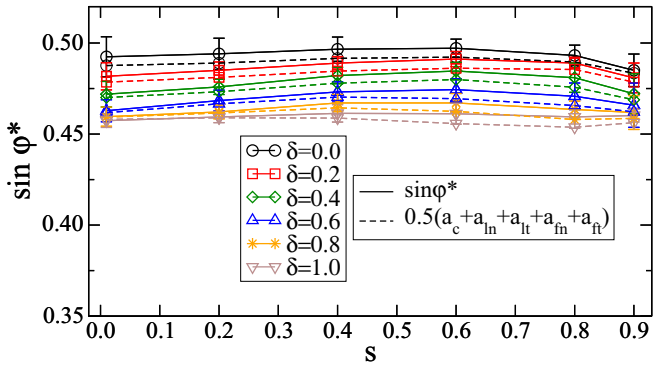

FIG. 12. (Color online) Normalized shear stress as a function of s for all values of δ (symbols and solid line) together with harmonic approximations given by Eqs. (11) (dashed line). Error bars correspond to the standard deviation of the fluctuations in the steady state.

and force transmission, but more fundamentally because they add together to build the shear strength of the material. Indeed, it can be shown that the general expression, (5), of the stress tensor leads to the following simple relation [7,12,39–41]:

$$\sin\varphi \simeq \tfrac{1}{2}(a_c + a_{\rm ln} + a_{\rm lt} + a_{\rm fn} + a_{\rm ft}). \qquad (12)$$

The predicted values of $\sin\varphi^*$ by this equation are shown in Fig. 12 together with the measured values as a function of s for all values of δ. We see that Eq. (12) approximates well the friction angle for all values of s and δ. By virtue of this equation, the independence of $\sin\varphi^*$ with respect to s is a consequence of the opposite variations of a_c and $a_{\ell\rm n} + a_{\rm fn}$ together with the fact that $a_{\rm ft}$ is independent of both s. On the other hand, the decrease in $\sin\varphi^*$ as a function of δ is due only to the decrease in a_c.

V. CONCLUSION

In this paper, a systematic investigation of the combined effects of size span and particle shape polydispersity in the quasistatic rheology of two-dimensional sheared granular media has been undertaken by means of CD simulations. We have worked with irregular pentagons characterized by a shape polydispersity parameter δ, representing the degree of deviation from a regular pentagon, and their size span s. The numerical samples were subjected to biaxial compression until a steady shear state without volume change was reached.

A central finding of this work is that the shear strength is independent of the size span but declines as the shape polydispersity increases. In contrast, the solid fraction increases in a strongly nonlinear manner with both size span and shape polydispersity. We have also performed a detailed analysis of the microstructure. In particular, the fabric and force anisotropies were analyzed as a function of the size and shape polydispersity.

The independence of shear strength with respect to size span was shown to be due to the falloff of geometrical anisotropy compensated by an increase in the normal force and branch anisotropies. This behavior is explained by the fact that strong force chains are captured by the largest particles. Schematically, the effect of increasing size span is to replace the larger particles with a growing population of smaller particles. The mean number of contacts around larger particles increases and leads to a decrease in contact anisotropy and an increase in branch and normal force anisotropies. We also evidenced a correlation between contact forces and branch vectors reflecting a subnetwork of very weak contacts with high friction mobilization and small branch vector lengths.

A similar mechanism was observed for the decrease in shear strength as a function of the shape polydispersity. The mean number of contacts around the largest particles increases with δ, reflecting the fact that the sharp corners of very irregular particles allow for more contact neighbors than with regular particles. As result, the contact orientation anisotropy declines with δ, thus leading to the decrease in shear strength.

To our best knowledge, this work is the first systematic investigation of shape polydispersity together with size polydispersity in granular materials. Our findings clearly show that an "average shape" is insufficient for modeling a granular material. The shear strength is affected by the dispersion of particle shapes, which control the local particle environments. The size span, on the contrary, has almost no effect on the shear strength as a result of the correlations between forces and particle sizes (or branch vector lengths). Hence, the particles may be represented by their "average size" as far as the shear strength is considered.

Such rather counterintuitive features suggest the necessity of further investigations of polydispersity effects with different particle shapes such as elongated and/or nonconvex shapes, in both two and three dimensions, in view of the realistic modeling of naturally occurring or manufactured granular materials. Complex particle shapes may be modeled through their contour surface or as aggregates composed of spherical particles. In molecular dynamics simulations, it is advantageous to work with aggregates, as the contact interactions between spheres are straightforward. But when the contours of particles involve plane faces, it is necessary to resort to special treatment of face-face contacts such as that employed in the present work in the framework of the CD method. In the same way, most natural granular materials involve cohesive contacts. According to the Mohr-Coulomb criterion, the shear strength of cohesive materials can be split into an internal angle of friction and a macroscopic cohesion, which reflects the aptitude of the material to sustain tensile stresses. An open issue is how the macroscopic cohesion is influenced by particle shape and size [43]. In all cases, three-dimensional simulations require a much larger number of particles compared to two-dimensional simulations for the sake of statistical representativity of size populations and, thus, a much more demanding computation time.

ACKNOWLEDGMENTS

This work was funded by the French Alternative Energies and Atomic Energy Commission (CEA). F.R. would also like to acknowledge the support of the ICoME2 Labex (ANR-11-LABX-0053) and the A*MIDEX (ANR-11-IDEX-0001-02) projects cofunded by the French program Investissements d'Avenir.

[1] A. Donev, I. Cisse, D. Sachs, E. Variano, F. Stillinger, R. Connelly, S. Torquato, and P. Chaikin, Science **303**, 990 (2004).

[2] C. Voivret, F. Radjaï, J.-Y. Delenne, and M. S. El Youssoufi, Phys. Rev. E **76**, 021301 (2007).

[3] E. Azéma, F. Radjai, R. Peyroux, and G. Saussine, Phys. Rev. E **76**, 011301 (2007).

[4] C. Voivret, F. Radjaï, J.-Y. Delenne, and M. S. El Youssoufi, Phys. Rev. Lett. **102**, 178001 (2009).

[5] I. Schenker, F. T. Filser, L. J. Gauckler, T. Aste, and H. J. Herrmann, Phys. Rev. E **80**, 021302 (2009).

[6] S. Torquato and Y. Jiao, Phys. Rev. E **80**, 041104 (2009).

[7] E. Azéma and F. Radjaï, Phys. Rev. E **81**, 051304 (2010).

[8] P. Sollich and N. B. Wilding, Phys. Rev. Lett. **104**, 118302 (2010).

[9] B. Saint-Cyr, K. Szarf, C. Voivret, E. Azéma, V. Richefeu, J.-Y. Delenne, G. Combe, C. Nouguier-Lehon, P. Villard *et al.*, Europhys. Lett. **98**, 44008 (2012).

[10] E. Azema and F. Radjai, Phys. Rev. E **85**, 031303 (2012).

[11] E. Azema, N. Estrada, and F. Radjai, Phys. Rev. E **86**, 041301 (2012).

[12] E. Azema, F. Radjai, and F. Dubois, Phys. Rev. E **87**, 062203 (2013).

[13] E. Azema, F. Radjai, B. Saint-Cyr, J.-Y. Delenne, and P. Sornay, Phys. Rev. E **87**, 052205 (2013).

[14] B. Zhou, R. Huang, H. Wang, and J. Wang, Granular Matter **15**, 315 (2013).

[15] V. Ogarko and S. Luding, Soft Matter **9**, 9530 (2013).

[16] T. Aste, Phys. Rev. E **53**, 2571 (1996).

[17] T. Aste and D. Weaire, *The Pursuit of Perfect Packing* (Institute of Physics, Bristol, UK, 2000).

[18] J. Mitchell and K. Soga, *Fundamentals of Soil Behavior* (Wiley, New York, 2005).

[19] M. Wackenhut, S. McNamara, and H. Herrmann, Eur. Phys. J. E **17**, 237 (2005).

[20] D.-H. Nguyen, E. Azéma, F. Radjai, and P. Sornay, Phys. Rev. E **90**, 012202 (2014).

[21] J. Moreau, Eur. J. Mech. A Solids **13**, 93 (1994).

[22] M. Jean, Comput. Methods Appl. Mech. Eng. **177**, 235 (1999).

[23] F. Radjai and V. Richefeu, Mech. Mater. **41**, 715 (2009).

[24] F. Radjai and F. Dubois (eds.), *Discrete Numerical Modeling of Granular Materials* (Wiley-ISTE, New York, 2011).

[25] L. Staron and F. Radjai, Phys. Rev. E **72**, 041308 (2005).

[26] G. Saussine, C. Cholet, P. Gautier, F. Dubois, C. Bohatier, and J. Moreau, Comput. Methods Appl. Mech. Eng. **195**, 2841 (2006).

[27] B. Saint-Cyr, J.-Y. Delenne, C. Voivret, F. Radjai, and P. Sornay, Phys. Rev. E **84**, 041302 (2011).

[28] N. Estrada, E. Azema, F. Radjai, and A. Taboada, Phys. Rev. E **84**, 011306 (2011).

[29] E. Azéma, Y. Descantes, N. Roquet, J.-N. Roux, and F. Chevoir, Phys. Rev. E **86**, 031303 (2012).

[30] E. Clement, Colloid Interf. Sci. **4**, 294 (1999).

[31] GDR-MiDi, Eur. Phys. J. E **14**, 341 (2004).

[32] J. J. Moreau, in *Friction, Arching, Contact Dynamics*, edited by D. E. Wolf and P. Grassberger (World Scientific, Singapore, 1997), pp. 233–247.

[33] C. Nouguier-Lehon, B. Cambou, and E. Vincens, Int. J. Num. Anal. Methods Geomech. **27**, 1207 (2003).

[34] C. Nouguier-Lehon, C.R. Mecan. **338**, 587 (2010).

[35] F. Radjai, D. E. Wolf, M. Jean, and J.-J. Moreau, Phys. Rev. Lett. **80**, 61 (1998).

[36] N. Estrada, A. Lizcano, and A. Taboada, Phys. Rev. E **82**, 011304 (2010).

[37] I. Zuriguel, T. Mullin, and J. M. Rotter, Phys. Rev. Lett. **98**, 028001 (2007).

[38] R. C. Hidalgo, I. Zuriguel, D. Maza, and I. Pagonabarraga, Phys. Rev. Lett. **103**, 118001 (2009).

[39] L. Rothenburg and R. J. Bathurst, Geotechnique **39**, 601 (1989).

[40] H. Ouadfel and L. Rothenburg, Mech. Mater. **33**, 201 (2001).

[41] E. Azéma, F. Radjai, and G. Saussine, Mech. Mater. **41**, 729 (2009).

[42] M. Boton, E. Azema, N. Estrada, F. Radjai, and A. Lizcano, Phys. Rev. E **87**, 032206 (2013).

[43] E. J. R. Parteli, J. Schmidt, C. Blümel, K.-E. Wirth, W. Peukert, and T. Pöschel, Sci. Rep. **4**, 6227 (2014).

[44] http://www.cgp-gateway.org/ref030.